

Two local slip modes at the liquid–liquid interface over liquid-infused surfaces

Cite as: Phys. Fluids **34**, 082017 (2022); doi: [10.1063/5.0098343](https://doi.org/10.1063/5.0098343)

Submitted: 8 May 2022 · Accepted: 26 July 2022 ·

Published Online: 17 August 2022








View Online



Export Citation



CrossMark

Liuzhen Ren (任刘珍),¹ Haibao Hu (胡海豹),^{1,a)}  Luyao Bao (鲍路瑶),^{2,3,a)}  Nikolai V. Priezjev,⁴  Jun Wen (谢络),¹ 
and Luo Xie (文俊)¹ 

AFFILIATIONS

¹School of Marine Science and Technology, Northwestern Polytechnical University, Xi'an, Shaanxi 710072, People's Republic of China

²State Key Laboratory of Solid Lubrication, Lanzhou Institute of Chemical Physics, Chinese Academy of Sciences, Lanzhou, Gansu 730000, People's Republic of China

³Shandong Laboratory of Yantai Advanced Materials and Green Manufacturing, Yantai, Shandong 264006, People's Republic of China

⁴Department of Mechanical and Materials Engineering, Wright State University, Dayton, Ohio 45435, USA

^{a)}Authors to whom correspondence should be addressed: huhaiobao@nwpu.edu.cn and baoluyao@licp.cas.cn

ABSTRACT

A liquid–liquid interface (LLI) at liquid-infused surfaces (LISs) plays a significant role in promoting slip flow and reducing frictional drag. By employing the transverse many-body dissipative particle dynamics simulations, the behavior of local and effective slip at a flat LLI for shear flows over periodically grooved LISs has been studied. With increasing viscosity ratio between the working fluid and lubricant fluid, two local slip modes are identified. For a small viscosity ratio, the local slip length remains finite along the LLI, while a hybrid local slip boundary condition holds along the LLI for large viscosity ratios, i.e., the local slip length is finite near the groove edge and unbounded in the central region of the LLI. The vortical flow inside the groove can be enhanced by increasing viscosity ratio due to the change in the local slip mode from the finite state to the hybrid one. Moreover, the results suggest two scenarios for the variation of the effective slippage. For LISs with a large LLI fraction, the effective slip length increases significantly with increasing viscosity ratio, while for a small LLI fraction, the effective slippage is rather insensitive to the viscosity ratio. The underlying mechanism for the relationship between the effective slip length and the viscosity ratio for different LLI fractions is revealed based on the two slip modes. These results elucidate the effect of LLI on slip boundary conditions and might serve as a guide for the optimal design of LISs with enhanced slip properties.

Published under an exclusive license by AIP Publishing. <https://doi.org/10.1063/5.0098343>

I. INTRODUCTION

In ocean engineering, drag reduction can significantly reduce energy consumption and enhance traveling speed or distance of underwater vehicles.^{1–3} Inspired by an unusual bounce behavior of water droplets on lotus leaves, superhydrophobic surfaces (SHSs) have been long explored to reduce flow drag.^{4–7} Due to the presence of micro- and nanostructures and relatively low surface energy of SHSs, air can be trapped within these structures when SHSs are submerged under water. As water is prevented from a direct contact with a solid wall, a gas–liquid interface (GLI) is formed to form an apparent slip, which makes SHSs useful for applications that require drag reduction.^{8–11}

Generally, the GLIs might suffer from the lack of stability.^{12,13} For instance, by using confocal microscopy, Lv *et al.* reported collapses of symmetric and asymmetric GLIs on a submerged SHS.¹⁴ Moreover, the collapse of a GLI can reduce the drag-reducing ability of SHSs or

even increase the flow drag. For example, Reholon *et al.*¹⁵ observed an apparent drag reduction of SHSs at lower Reynolds numbers, but the drag reduction rate decreased at higher Reynolds numbers, similar to the observations of Xu *et al.*¹⁶ In fact, not only flow-induced shear but also air dissolution^{17,18} or pressure fluctuation^{19,20} can make the GLIs unstable.

Although Xu *et al.* achieved an increase in lifetime of 120 h for SHSs by minimizing environmental factors,¹⁷ it is hardly possible to indefinitely keep the superhydrophobic state under realistic conditions. So, the stability of GLIs over SHSs has to be continuously maintained. By combining air injection and surface hydrophobicity adjustment, Du *et al.* clearly demonstrated a recovery of an air layer on SHSs and the appearance of slip flow.²¹ Several novel methods including water electrolysis,^{22,23} decomposition reaction of hydrogen peroxide,²⁴ the Leidenfrost effect,^{25,26} and a specific doubly reentrant structure²⁷ were

also used to generate or maintain a gas layer over SHSs. Based on the wettability step effect, Hu *et al.* created novel SHSs to maintain a large-scale gas film and obtained a drag reduction rate as large as 77.2% in a Taylor–Couette flow apparatus.²⁸

On the other hand, the liquid-infused surfaces (LISs), which are inspired by the Nepenthes pitcher plants, have been recently fabricated and shown to exhibit interfacial slip.^{29,30} Similar to the SHSs, the LISs are also manufactured with micro- and nanostructures and reduced surface energy, but a liquid lubricant (instead of a gas layer) is infused within these structures. Recently, Solomon *et al.* demonstrated that drag reduction of LISs depends on the viscosity ratio between the working fluid and the lubricant.³¹ Specifically, it was shown that for laminar flow conditions and the viscosity ratio of 260, the drag was reduced by 16%. More recently, Rosenberg *et al.* have suggested that LISs may enable robust drag reduction in turbulent flows.³² They also reported a drag reduction rate that was exceeded 35% for LISs and demonstrated that drag reduction increased with increasing viscosity ratio, groove width, fluid area, and Reynolds number.³³

There are three criteria to design slippery LISs:^{34,35} (1) the lubricant liquid should wick into, wet, and stably adhere within the substrate, (2) the solid must be preferentially wetted by the lubricant liquid rather than by the working liquid that needs to be repelled, and (3) the lubricant fluid and working fluid must be immiscible. Since the lubricant is always insoluble in water when the LISs are submerged under water, the LLI is more stable than the GLI and, thus, becomes more advantageous for drag reduction.^{33,36} For example, Tuo *et al.* found that the LIS can repair itself and restore the drag reduction effect even if a small amount of lubricant oil is impregnated into the porous substrate.³⁷ By comparing drag-reducing abilities before and after several instances exposure to a high shear flow, a biomimetic LIS fabricated by Sang *et al.* performed an excellent sustainability as it exhibited a minimal decrease in the drag-reducing capability.³⁸ In addition, a novel chemical technique,³⁹ a small amount of surfactant,⁴⁰ or random roughness of superhydrophobic PTFE surfaces⁴¹ can enhance retention of a lubricant and maintain the drag-reducing ability of LISs.

When a lubricant is infused into structured substrates, the original solid–liquid interface (SLI) is replaced by a liquid–liquid interface (LLI) on submerged LISs, which is the key for interfacial slip and drag reduction. For example, by directly measuring the slip length over a biomimetic LIS, Sang *et al.* observed drag reduction by 18%, while this effect was absent for the no-slip surface.³⁸ More recently, it was shown numerically that the maximum values of local slip velocity and slip length have occurred in the center of the contact interface, which formed a paraboloid at the LLI.⁴² Furthermore, Asmolov *et al.* demonstrated that the effective slip length increased with the LLI fraction and the viscosity ratio, whereas the influence of the protrusion angle was insignificant.⁴³ Assuming Stokes flow, Chang *et al.* proposed a model for drag reduction at the heptane-lubricated surface.³⁰ Interestingly, for the LISs with trapped air, Hemeda *et al.* predicted a drag reduction by 20%–37% when compared with a traditional LIS.⁴⁴ Despite a significant progress in the fabrication and characterization of LISs, the relationship between slip boundary conditions and properties of LLI has remained not fully understood.

Recently, we have derived a hybrid slip boundary condition at a flat GLI over periodically grooved SHSs, based on many-body dissipative particle dynamics (MDPD) simulations.¹⁰ It is the local shear

stress and the local slip length that are finite near the groove edge, while the stress is nearly zero and the slip length appears to be infinite in the central region of the GLI. As the MDPD simulation method proved to be useful to simulate multiphase flows,^{45–49} it is applied in this study to explore the slip behavior over LISs and to examine whether a hybrid slip boundary condition is more appropriate along the LLI. In addition, the effects of the LLI fraction and the viscosity ratio between the working liquid above the LISs and the lubricant infused in surface structures on the slip behavior over LISs are studied.

The recent research about the drag-reducing ability and slip property of LIS are briefly introduced in this Sec. I. The remainder of this paper is organized as follows. Section II describes the simulation method, which consists of the modified MDPD scheme, simulation setup, and model parametrization. By introducing a flat LLI over LISs, the slip properties of the LLI are investigated for different viscosity ratios and LLI fractions in Sec. III. Finally, a summary of the results and our conclusions are presented in Sec. IV.

II. SIMULATION METHODS

A. MDPD scheme

In the standard MDPD (S-MDPD) simulations, as particles interact via three pairwise forces along the interparticle axis, the S-MDPD thermostat cannot effectively control the liquid viscosity.⁵⁰ Recently, a new transverse MDPD (T-MDPD) scheme was proposed to tune the viscosity of a MDPD fluid over a wide range.⁵¹ With a lateral friction coefficient added to the S-MDPD form, the three pairwise forces, namely, the conservative, dissipative, and random forces, are redefined as follows:

$$\mathbf{F}_{ij}^C = [A_{ij}\omega_c(r_{ij}) + B_{ij}(\bar{\rho}_i + \bar{\rho}_j)\omega_d(r_{ij})]\mathbf{e}_{ij}, \quad (1)$$

$$\mathbf{F}_{ij}^D = -\gamma^\parallel\omega_D^\parallel(r_{ij})(\mathbf{e}_{ij} \cdot \mathbf{v}_{ij})\mathbf{e}_{ij} - \gamma^\perp\omega_D^\perp(r_{ij})[\mathbf{v}_{ij} - (\mathbf{e}_{ij} \cdot \mathbf{v}_{ij})\mathbf{e}_{ij}], \quad (2)$$

$$\mathbf{F}_{ij}^R = \sigma^\parallel\omega_R^\parallel(r_{ij})(\mathbf{e}_{ij} \cdot \boldsymbol{\theta}_{ij})\mathbf{e}_{ij} + \sigma^\perp\omega_R^\perp(r_{ij})[\boldsymbol{\theta}_{ij} - (\mathbf{e}_{ij} \cdot \boldsymbol{\theta}_{ij})\mathbf{e}_{ij}]. \quad (3)$$

In the definition of \mathbf{F}_{ij}^C , A_{ij} is the strength of the attractive force and B_{ij} is the strength of the repulsive force. r_{ij} is the distance between particles i and j , $\mathbf{e}_{ij} = (\mathbf{r}_i - \mathbf{r}_j)/r_{ij}$ is the unit vector in the direction from particle j to i , and \mathbf{r}_i represents the position vector of particle i . $\omega_c(r) [= (1 - r/r_c)]$ and $\omega_d(r) [= (1 - r/r_d)]$ are weight functions that vanish for $r > r_c$ and $r > r_d$, respectively, and r_c and r_d are cutoff radii of the attractive and repulsive forces, respectively. Thus, the attractive force between the particles i and j varies linearly with r_{ij} while r_{ij} is less than r_c . $\bar{\rho}_i = \sum_{i \neq j} \omega_\rho(r_{ij})$ is the local density for each particle within the effective range r_d , where $\omega_\rho(r) = [105(1 + 3r/r_d)(1 - r/r_d)^3]/(16\pi r_d^3)$ is the weight function.

In Eqs. (2) and (3), γ and σ are friction coefficients and random coefficients, respectively. Specifically, γ^\parallel and σ^\parallel are the components along the direction of \mathbf{e}_{ij} , whereas γ^\perp and σ^\perp are the components perpendicular to that direction. Meanwhile, the coefficients satisfy the relation $\sigma^2 = 2\gamma k_B T$ for both of these two directions. Here, k_B is the Boltzmann constant and T is the temperature of the system. The weight functions are set as $\omega_D^\parallel(r) = \omega_D^\perp(r) = (1 - r/r_c)^2$, where r_c is the interaction range. The weight functions $\omega_R^\parallel(r) = \omega_R^\perp(r)$ are chosen such that $\omega_D(r) = [\omega_R(r)]^2$. Additionally, $\mathbf{v}_{ij} = \mathbf{v}_i - \mathbf{v}_j$ is the velocity difference, where \mathbf{v}_i and \mathbf{v}_j are the velocities of particles i and j .

In Eq. (3), θ_{ij} is a three-dimensional vector that its elements are independent Gaussian random numbers with zero mean and unit variance. This vector satisfies the following conditions:

$$\langle \theta_{ij} \rangle = 0, \tag{4}$$

$$\theta_{ij}(t) \otimes \theta_{kl}(t') = \mathbf{I}(\delta_{ik}\delta_{jl} - \delta_{il}\delta_{jk})\delta(t - t'), \tag{5}$$

where \mathbf{I} is a 3×3 matrix and \otimes represents the dyad product. When $\gamma^\perp = \sigma^\perp = 0$ in the T-MDPD scheme, the standard form is recovered. In an MDPD system, the governing equation for the i th particle is given by

$$m_i \frac{d^2 \mathbf{r}_i}{dt^2} = \sum_{i \neq j} \mathbf{F}_{ij}^C + \mathbf{F}_{ij}^D + \mathbf{F}_{ij}^R. \tag{6}$$

B. Simulation setup

Figure 1 shows a schematic illustration of the simulation setup. The channel is confined between the upper and lower walls with the dimensions of L_x ($= 64.0$ in the DPD units) in the x -direction, L_y in the y -direction, and L_z ($= 8.0$ in the DPD units) in the z -direction. In addition, a rectangular groove, with a height h ($= 31.89$ in the DPD units), length L_z , and width w , is carved inside the lower wall. Note that the MDPD method operates in reduced DPD units for convenience, the map between the DPD units and the physical units is

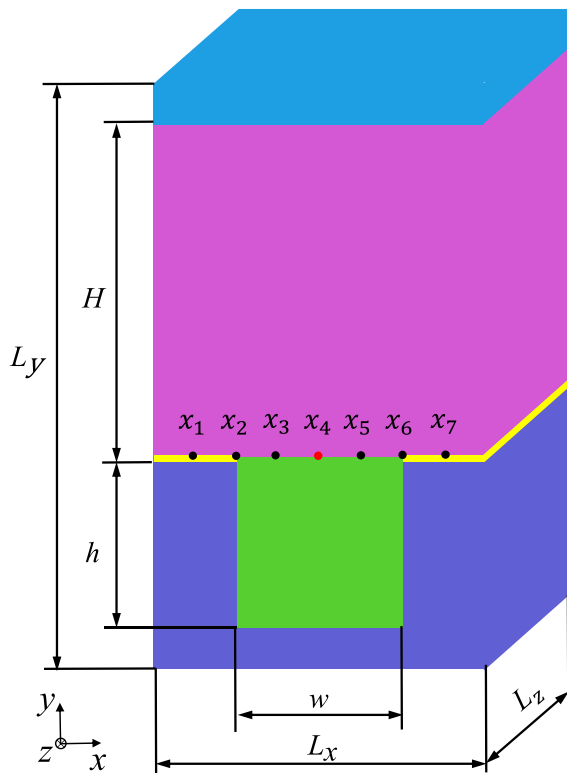


FIG. 1. A schematic representation of the simulation setup. H is the height of the channel, L_x and L_z are the sides of the LIS, and h and w are the depth and width of the groove, respectively.

instructive to a specific set of properties of a real liquid, and the detail will be discussed later in Sec. II C. A Newtonian liquid (the working fluid) is confined in the channel, while the groove is filled with another immiscible liquid (the lubricant liquid) to simulate a liquid-infused surface (LIS). By adjusting the channel height (H), the shape of the liquid–liquid interface (LLI) is controlled as described in literature.¹⁰ The LLI is intentionally made to be flat in this study. The width w is varied to simulate LISs with different fluid interface fractions.

With a lateral friction coefficient added to the S-MDPD form, the viscosity of the T-MDPD fluid is much higher than that of a S-MDPD fluid, and it is sensitive to the transverse friction coefficient, as shown in literature.⁵¹ While the particle number density of the working fluid and the lubricant fluid are set in the DPD units to $\rho_w = 6.74$ and $\rho_l = 3.24$, respectively, the viscosities of these two types of T-MDPD fluids are primarily adjusted by the friction coefficient. Then, the viscosity ratio between the working fluid and the lubricant fluid varies over a wide range, which exceeds the range for a classical SHS with air trapped in surface structures, as described in Sec. III.

In the simulations, the upper wall, lower wall, and the two types of T-MDPD liquids are initially constructed from the face-centered cubic crystal. With a particle density number of 12.0 in the DPD units, the upper wall consists of 19 980 solid particles. When w is equal to 15.60, 23.57, 31.55, 39.52, and 47.50 in the DPD units, the lower wall, with the same density as the upper wall, consists of 177 876, 152 484, 127 092, 101 700, and 67 428 particles, respectively. At the same time, the number of liquid particles in the groove is 12 615, 18 705, 25 230, 31 755, and 37 845, respectively, while the working fluid always consists of 203 889 particles.

In order to form a stable LLI over the LIS, the particles of the working fluid are made to repel the lubricant fluid, while a no-slip boundary condition is applied at the channel’s solid surfaces (the upper wall and the topmost layer of the lower wall). In the setup, the lower wall is kept stationary, while the upper wall is translated with a constant velocity U_x in the $+x$ direction to generate a transverse shear flow with respect to the groove. Periodic boundary conditions are applied along the x - and z -directions to simulate a periodic array of grooves. The coordinate origin is located at the center of the LLI as x_4 (Fig. 1), and the individual positions of x_1 – x_7 are $-0.375 L_x$, $-0.25 L_x$, $-0.125 L_x$, 0.0 , $0.125 L_x$, $0.25 L_x$, and $0.375 L_x$, respectively.

C. MDPD Parameters

The interaction parameters used in the current study are listed in Table I in the DPD units. These are the representative values for a multiphase flow in an MDPD system.^{52–54} The subscripts w and l denote the working fluid in the channel and the infused liquid in the groove, respectively. In addition, the subscripts l and s denote the liquid (working fluid and lubricant fluid) and the solid wall, respectively.

The attraction coefficient between the working fluid and the channel walls (the upper wall and the topmost layer of the lower wall) is set to -40.0 to achieve a no-slip boundary. This coefficient between the working fluid and the groove walls is set to -4.0 to prevent the working liquid from wetting grooves. Meanwhile, it is also set as -4.0 between the working fluid and the lubricant to make them highly immiscible.⁵⁵ The attraction coefficient is zero between the lubricant particles to simulate a light fluid, while it is -40.0 between the particles of the working fluid to simulate a heavy fluid. The mapping relations between the physical and the DPD units for the length, mass, and time

TABLE I. Parameters in the DPD units used in this study.

Parameter	Symbol	Value
Particle number density of the working fluid	ρ_w	6.74
Particle number density of the infused lubricant	ρ_i	3.24
Attraction coefficient	$A_{ww} = A_{ss}$	-40.00
Attraction coefficient	A_{ii}	0.00
Repulsion coefficient	$B_{ll} = B_{sl} = B_{ss}$	25.00
Cutoff radius of the attractive force	r_c	1.00
Cutoff radius of the repulsive force	r_d	0.75
Friction coefficient	$\gamma_{sl} = \gamma_{ss}$	18.00
System temperature	k_{BT}	1.00
Time step	Δt	0.01

are $l^{phy} = [L] \times l^{DPD}$, $m^{phy} = [M] \times m^{DPD}$, and $t^{phy} = [T] \times t^{DPD}$, respectively. Here, the quantities in square brackets denote the scaling relationship between the physical and DPD quantities, which are based on the density, viscosity, and surface tension of the T-MDPD fluid.

In this study, both friction coefficients for the working and lubricant fluids are varied to provide different viscosity ratios. Here, taking a classical simulation case, where the friction coefficient of the working fluid is 50.0 and it is 2.0 for the lubricant fluid, we find the mapping relations between the physical and the DPD units. Note that the friction coefficients along the two directions (as described in Sec. II A) are the same for a pair of particles in current simulations. By applying the Poiseuille flow method,^{51,56,57} the viscosities of these two types of T-MDPD fluids were obtained as $\mu_w = 74.31$ and $\mu_i = 1.22$ in the DPD units, which provides a maximum value of 60.77 for the viscosity ratio. Based on the Irving–Kirkwood equation,^{58,59} the surface tension of the

working fluid Γ_{ww} is 12.76 in the DPD units. Comparing density, viscosity, and surface tension of the current T-MDPD fluid with physical water,⁶⁰ the scaling factors for the length, mass, and time are obtained as $[L] = 2.16 \times 10^{-10}$ m, $[M] = 1.49 \times 10^{-27}$ kg, and $[T] = 5.14 \times 10^{-13}$ s, respectively. Taking $U_x = 0.50$ and a typical value $w = 15.60$, the capillary number $Ca (= \mu_w \bar{\gamma} w / \Gamma_{ww})$, where $\bar{\gamma} = U/H$ is the average shear rate in the channel) is 0.76. The upper estimate of the Reynolds number $Re (= \rho_w U_x H / \mu_w)$ is 2.69, indicating laminar flow conditions. Thus, the interface is considered to be steady during simulations.

With a time step Δt of 0.01 in the DPD units, all simulations are carried out using the open-source LAMMPS MD code.⁶¹ Before production runs, the number of time steps for the initial equilibration is 5.0×10^5 . After equilibration, the transverse shear flow is generated and developed to a steady state during 1.0×10^6 steps. The entire simulation box is then divided into narrow bins, with $\Delta x = 1.0$ and $\Delta y = 1.0$ in the DPD units parallel to the x - z plane, and the density and velocity fields of the fluid both in the channel and in the groove are computed by averaging over 1.0×10^6 time steps.

III. RESULTS AND DISCUSSION

A. Local flow field over LISs

In this study, a set of system parameters are considered that resulted in a flat LLI. As shown in Fig. 2(a), the shape of the interface was controlled by suitably adjusting the channel height. Specifically, the location of the LLI was defined at the position where the local particle density is equal to half of the sum of the liquid densities in the channel and in the groove. By fitting the normal profile of the local density using a hyperbolic tangent function along the stream-wise direction, a series of independent locations of the LLI were computed. These locations were fitted using a polynomial function to smoothen the shape of the LLI, as indicated by the black dashed curves in Fig. 2(a).

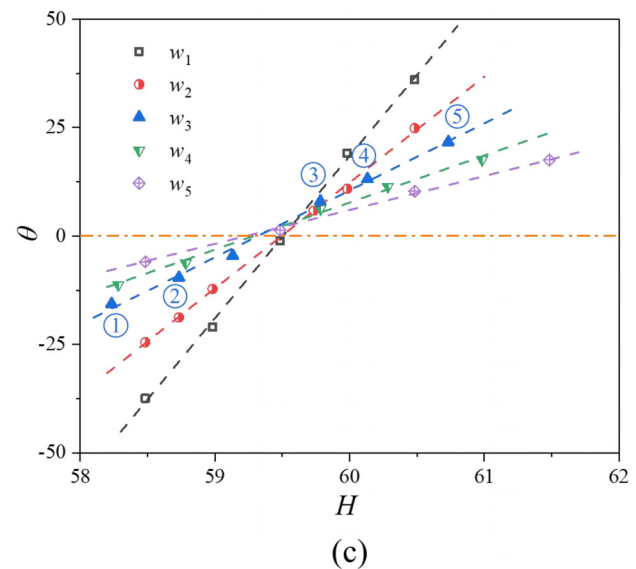
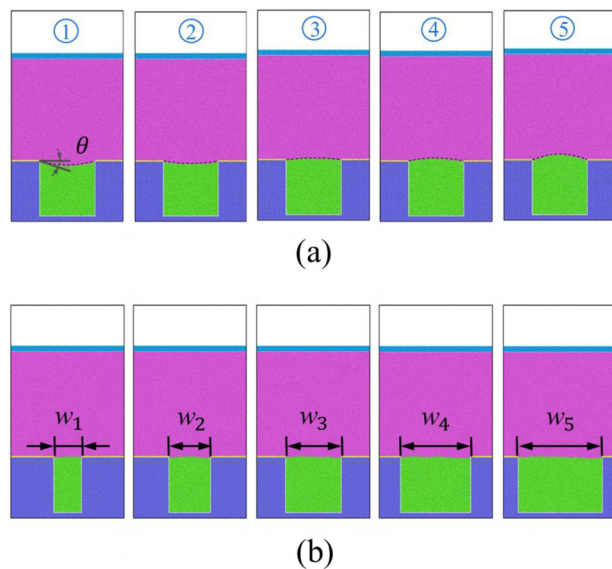


FIG. 2. (a) The shape of the LLI for different values of the channel height H (the groove width $w = w_1$), (b) flat LLIs for various groove widths w , and (c) the contact angle θ as a function of H for the indicated values of w ($w_1 = 15.60$, $w_2 = 23.57$, $w_3 = 31.55$, $w_4 = 39.52$, $w_5 = 47.50$, $\gamma_{ww} = 50.0$, and $\gamma_{ii} = 18.0$).

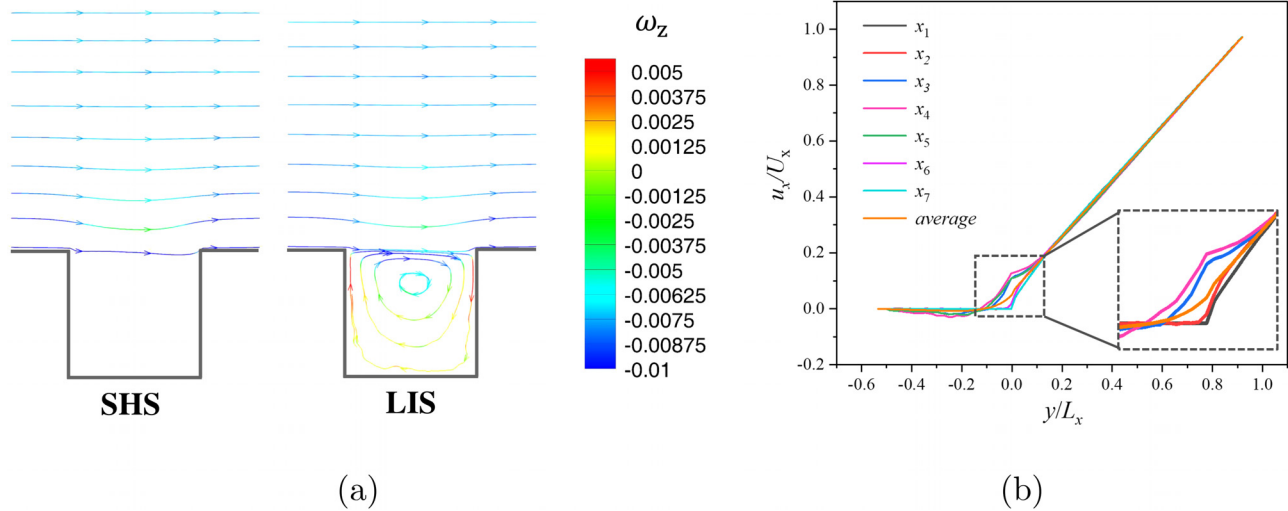


FIG. 3. Flow fields at the LIS: (a) streamline patterns and (b) normalized profiles of the local streamwise velocity u_x along the y -direction ($w = 31.55$ and $N = 17.62$). In the panel (a), the thick black lines represent groove walls, the “SHS” denotes an idealized SHS with an empty groove, the color code indicates the vorticity ω_z along the z -direction. In the panel (b), only the profiles of positions x_1 to x_4 and the average profile are included in the inset, and U_x is the upper wall speed.

For given groove width w and DPD settings, the contact angle (θ) at the groove edge depends on the channel height H [Fig. 2(a)]. For a convex LLI, i.e., the LLI is protruded into the channel, θ is positive, while it is negative for a concave LLI. Consequently, by plotting θ as a function of H for the fixed system parameters, a channel height (H_0) that corresponds to $\theta = 0$ was determined [Fig. 2(c)]. Then, by setting $H = H_0$, a flat LLI was obtained for different values of w [Fig. 2(b)].

The flow field for a flat LLI with $w = 31.55$ in the DPD units is shown in Fig. 3. The friction coefficients were set to 50.0 and 18.0 for the working fluid and the lubricant fluid, respectively, which results in the viscosity ratio of $N = 17.62$. As shown in Fig. 3(a), the presence of the lubricant in the groove changes the flow field at the LIS and leads to a vortical flow in the groove. Furthermore, the normal profiles of the local streamwise velocity (u_x) are presented in Fig. 3(b). Specifically, u_x was computed by averaging over narrow bins with a width of 1.0 in the DPD units along the x -direction and a height of 1.0 in the DPD units along the y -direction. The velocity profiles were normalized by the corresponding upper wall speed U_x . Here, $y = 0$ denotes the location of the LLI, and x_{es} are individual locations along the x -direction (Fig. 1).

The velocity profiles above the SLI correspond to the positions x_1 or x_7 [Fig. 3(b)]. It can be clearly seen that the velocity varies almost linearly with y and it is zero at the SLI. In the near-LLI region, the normal profiles of the streamwise velocity (u_x) become curved right above the LLI while x varies from x_2 to x_6 . These observations demonstrate an apparent slippage at the LLI. Note that the normal profiles of u_x is the highest in the center of the LLI, i.e., at x_4 . In addition, the velocity profiles are almost symmetric about the center, e.g., the normal profiles of u_x at x_3 and x_5 . From the location of the LLI, as y gradually increases into the bulk region, the velocity gradient increases. Further away from the interface, the velocity profiles nearly collapse into each other and increase linearly as a function of y , implying that the influence of the LLI becomes relatively small.

As shown in Fig. 3(a), the vortical flow inside the groove is induced by the stress at the LLI from the working fluid. Moreover, as indicated in Fig. 4, the working fluid and lubricant slip pass each other along the LLI. Here, the apparent slip velocity (u_s) was computed by averaging inside narrow bins at the interface, and actually, it is the velocity of the working fluid at the LLI. In our recent study on slip flow over SHSs, a new fitting method was proposed to analyze the local shear stress and the local slip length.¹⁰ By applying this method in this study, the normal profiles of the local velocity were also fitted using a fifth order polynomial function to extract the velocity gradient. The local shear stress (τ) and the local slip length (l_s) were then

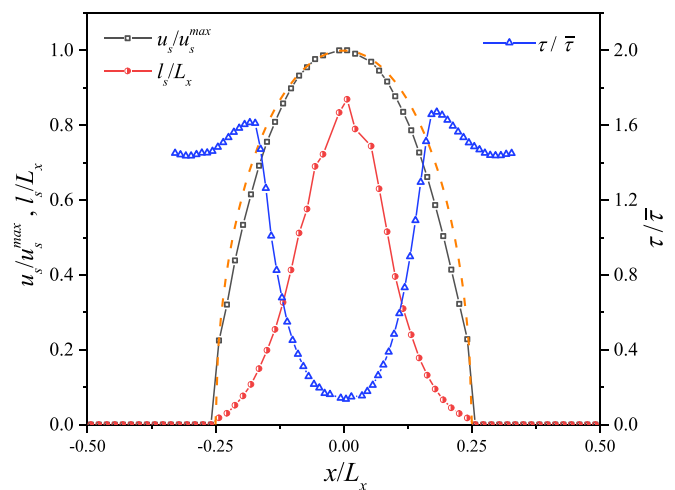


FIG. 4. The local slip velocity u_s (black squares), local slip length l_s (red circles), and local shear stress τ (blue triangles) along the LLI at LIS ($w = 31.55$ and $N = 17.62$). The dashed orange curve represents a fit using an elliptical function.

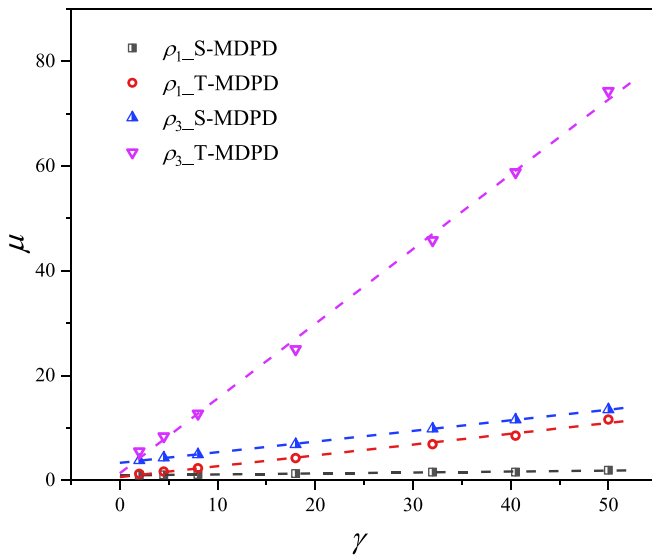


FIG. 5. The dependence of the viscosity μ as a function of the friction coefficient γ for the MDPD fluid ($\rho_1 = 6.74$, $\rho_3 = 3.24$).

computed based on the Newton’s law of viscosity and the Navier slip model, respectively.

In Fig. 4, u_s is normalized by the maximum slip velocity (u_s^{\max}) at the center of the LLI, l_s is normalized by the system size L_x , and τ is normalized by the average shear stress $\bar{\tau} = \mu U_x/H$, where μ is the viscosity of the working fluid. It was found that profiles of u_s , τ , and l_s are symmetric near the center of the LLI, while u_s and l_s are both larger at the center of the LLI where τ is reduced. More specifically, u_s is always positive along the LLI whereas u_s is zero along the SLI due to the imposed no-slip boundary condition. Figure 4 also shows that the normalized velocity profile is well described by the elliptical function

$$u_s/u_s^{\max} = \sqrt{1 - (x/(L_x/4))^2}.$$

As shown in Fig. 4, upon varying x from the groove edge to the center of the LLI, τ gradually decreases while l_s increases. These trends are consistent with the variation of the local slip over SHSs. This decrease in the local shear stress and the corresponding increase in the local slip length emphasize the effectiveness of LISs in reducing frictional drag. Note that in contrast to flow over periodically grooved SHSs, where the local l_s is finite near the groove edge and is infinite at the center region of the LLI, the local l_s remains finite at the LLI while flow over periodically grooved LISs. As a result, a finite slip boundary condition at LISs is more appropriate than the hybrid slip boundary condition, which was proposed in our recent study on flows over SHSs.¹⁰

B. The effect of viscosity ratio on interfacial slip

The influence of the viscosity ratio, between the working fluid and lubricant, on the local slippage at the LLI and flow patterns inside the groove and above the LIS is then examined. First, the friction coefficient γ , along two directions was systematically varied to investigate its influence on fluid viscosity. The results are presented in Fig. 5. In comparison with the S-MDPD fluid, the viscosity of the T-MDPD fluid becomes more sensitive to the friction coefficient γ . As γ increases from 2.0 to 50.0, the viscosity varies from 5.51 to 74.31 in the DPD units for the fluid in the T-MDPD scheme, while it only changes from 3.78 to 13.51 in the DPD units for the S-MDPD fluid for the same particle density of 6.74 in the DPD units.

Next, γ is fixed at a value of 50.0 for the working fluid, as γ varied from 2.0 to 50.0 for the lubricant fluid, the viscosity ratio (N), thus, changed from 60.77 to 6.41. The streamline patterns over LISs for several values of N are displayed in Fig. 6. It should be noted that the viscosity ratio $N_2 = 56.25$ was used to simulate a classical SHS with trapped air.^{30,62} The results in Fig. 6 show that the presence of the lubricant affects flow above the LIS, and the shear stress at LLI induces a vortex flow inside the grooves. Note that upon increasing N , the z -vorticity in the grooves becomes more pronounced.

The normal profiles of the local streamwise velocity u_x at the center of the LLI for the indicated values of N are shown in Fig. 7.

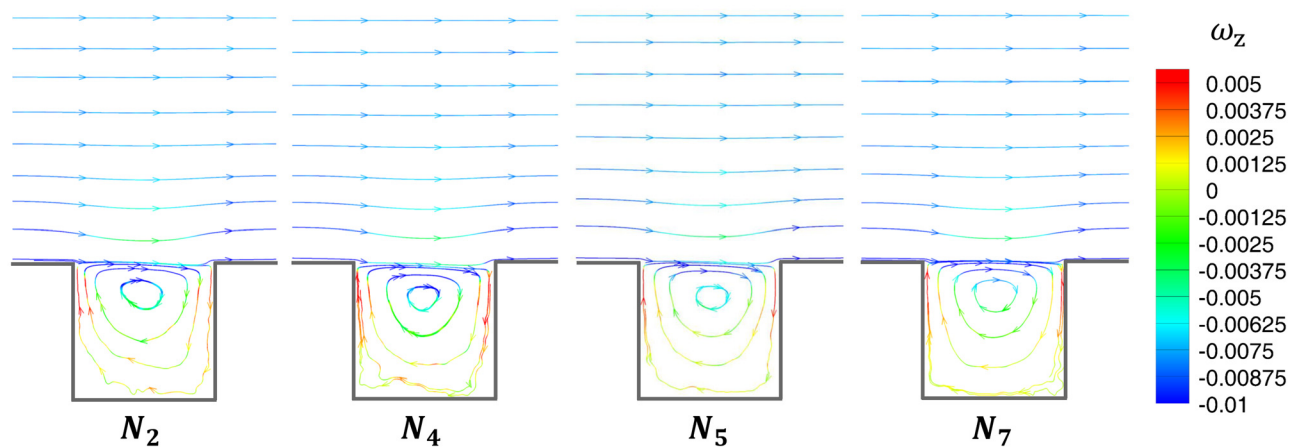


FIG. 6. Illustration of the streamline patterns over LISs for different viscosity ratios N ($w = 31.55$, $N_2 = 56.25$, $N_4 = 32.45$, $N_5 = 17.62$, and $N_7 = 8.74$). The color code indicates the vorticity ω_z along the z -direction.

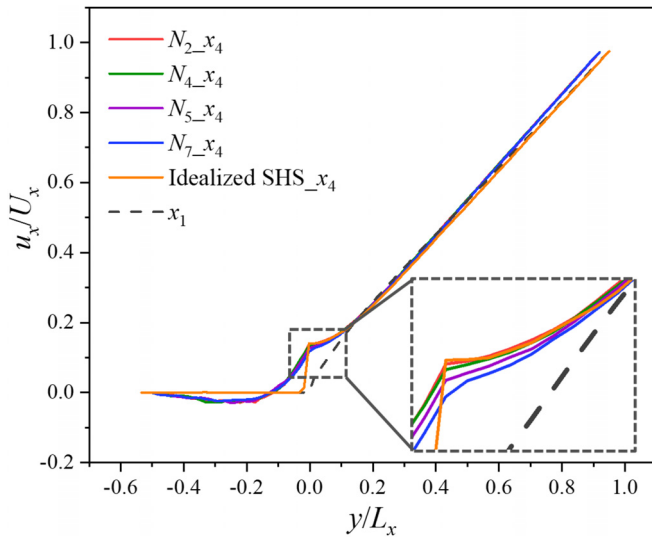


FIG. 7. The normal profiles of the local streamwise velocity u_x at LISs for different viscosity ratios N (x_4 denotes the center of the LLI, x_1 indicates the center of the SLI, $w = 31.55$, $N_2 = 56.25$, $N_4 = 32.45$, $N_5 = 17.62$, and $N_7 = 8.74$). U_x is the upper wall speed.

For reference, the velocity profile for an idealized SHS is also included in Fig. 7. As shown in Fig. 7, the velocity near the interface is larger for the idealized SHS (orange) than for LIS, even when N approaches the viscosity ratio of a classical SHS. With decreasing N , the velocity gradually decreases near the interface while the velocity profiles at the bulk region become nearly identical.

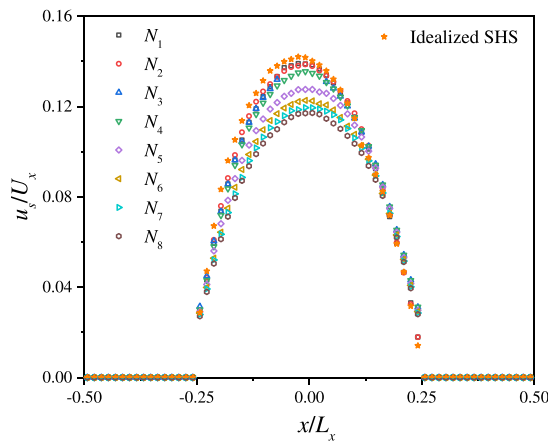
The local slip velocity (u_s) along the LLI for different viscosity ratios N is plotted in Fig. 8(a). It can be seen that u_s increases with increasing N , and u_s at LLIs is smaller than that at the GLI, which is consistent with the results for the local streamwise velocity, shown

in Fig. 7. Note that the difference between LLI and GLI becomes more pronounced at the center of the fluid interface. As shown in Fig. 8(b), when u_s is normalized by the corresponding maximum slip velocity at the center of the LLI over LISs (or GLI over SHSs), the normalized velocity profiles closely follow the elliptical function $u_s/u_s^{\max} = \sqrt{1 - (x/(L_x/4))^2}$.

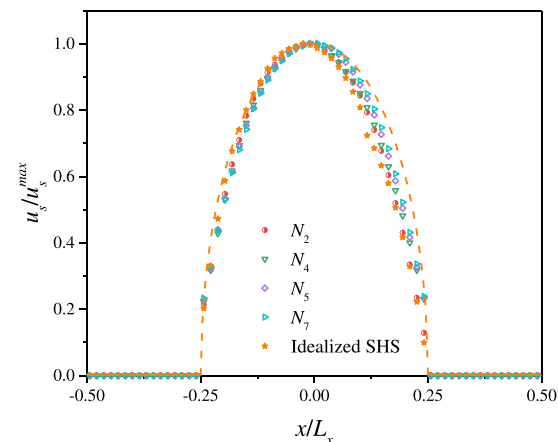
The local shear stress τ that was computed from the normal profiles of the local streamwise velocity is shown in Fig. 9(a). With increasing N , τ gradually decreases, leading to enhanced drag reduction. Simultaneously, the local slip length l_s increases [Fig. 9(b)]. Note that l_s becomes much larger than the system size at the central region of the LLI when N increases up to 56.25. Although l_s is smaller than l_s for an idealized SHS, the profiles of the local shear stress and the slip length at the LLI with a relatively large value of N are similar to those at a GLI, indicating that a hybrid slip boundary condition holds at the fluid interface.

Therefore, a hybrid slip mode applies at the LLI over LISs for larger N , where a finite local slip is present near the groove edge and an infinite slip occurs at the center of the LLI. At smaller N , both the local shear stress and the slip length remain finite along the LLI, and a finite slip boundary condition can be assumed. This transition in the local slip mode upon increasing N leads to a higher vorticity of the flow in the groove.

The results in Fig. 5 show that the increase in the friction coefficient and a higher liquid particle density both contribute to an increase in viscosity of a T-MDPD fluid. Here, the friction coefficient of the working fluid (γ_{ww}) is first varied to modify the viscosity ratio (N). For a given lubricant fluid, where the friction coefficient γ_{ii} and particle density ρ_i are fixed, the viscosity of the working fluid reduces with decreasing γ_{ww} , which consequently causes a decrease in N and l_s [Fig. 10(a)]. Moreover, the particle density of the lubricant fluid ρ_i was varied. As the friction coefficient γ_{ww} and the particle density ρ_w are kept fixed for the working fluid, the increase in ρ_i also reduces N and l_s [Fig. 10(b)]. For example, when γ_{ii} is set to 8.0, the maximum slip



(a)



(b)

FIG. 8. The local slip velocity u_s along LLIs for different viscosity ratios N : (a) normalized by the upper wall speed U_x ; (b) normalized by the maximum slip velocity u_s^{\max} ($w = 31.55$, $N_1 = 60.77$, $N_2 = 56.25$, $N_3 = 45.02$, $N_4 = 32.45$, $N_5 = 17.62$, $N_6 = 10.81$, $N_7 = 8.74$, and $N_8 = 6.41$). The dashed orange curve in the panel (b) represents a fit using an elliptical function.

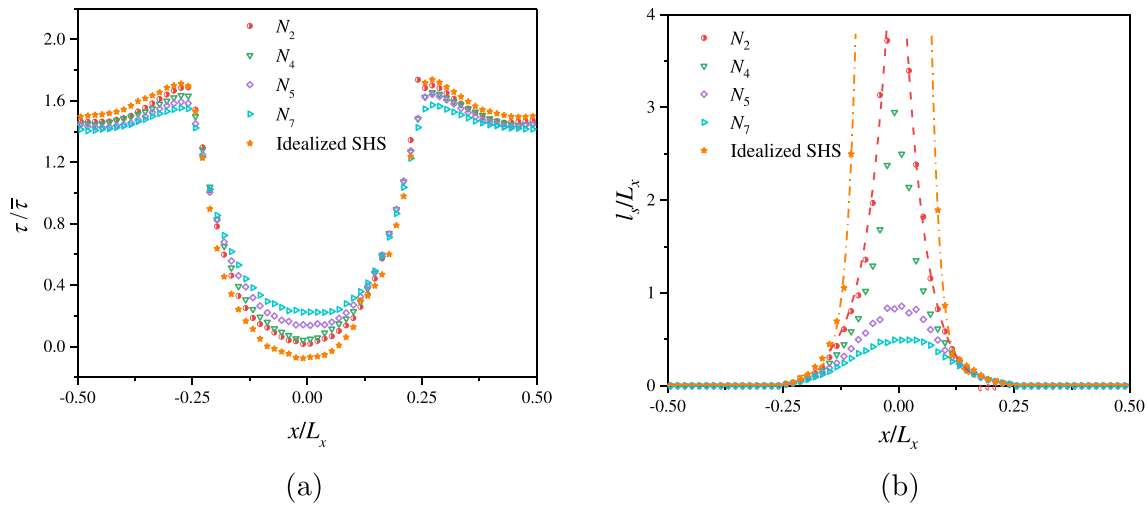


FIG. 9. (a) The local shear stress τ and (b) local slip length l_s at the LLI for different viscosity ratios N ($w = 31.55$, $N_2 = 56.25$, $N_4 = 32.45$, $N_5 = 17.62$, and $N_7 = 8.74$). The dashed curves in the panel (b) indicate the exponential fittings to l_s .

length in the center of the LLI decreases from $2.95 L_x$ to $0.97 L_x$, while ρ_i increases from 3.24 to 4.32 in the DPD units.

C. Effective slippage over LISs

While a detailed description of slip flow near the LLI over LISs involves a local slip length, the flow far away from the LISs is characterized by the effective slip length. This effective slip length relates the mean velocity at the interface and the shear rate in the bulk region. By assuming vanishing viscosity of a fluid filling surface corrugations, an expression for the effective slip length at the GLI for a transverse flow was originally derived by Philip.^{63,64} However, this expression might not always hold for LISs, since the viscosity of the infused fluid significantly affects the shear stress at the LLI. More recently, by taking into

account the viscosities of both fluids, Schönecker *et al.* obtained analytical predictions for the flow field and the effective slip length at LISs.⁶²

Although Schönecker *et al.*'s analysis describe the influence of an entrapped fluid on the flow over a LIS, the analytical derivation of the effective slip length is rather involved. Here, the effective slip length (l_{es}) was directly measured as follows: the normal profiles of the streamwise velocity (in the x -direction) in the bulk region were first averaged along the entire channel, the averaged velocity profile was then linearly extrapolated to the location of the LLI to determine the effective slip velocity and the velocity gradient, and thus, the effective slip length was calculated based on the Navier slip model.

It should be noted that in both Philip's and Schönecker *et al.*'s analyses, the effective slip length (l_{es}) over grooved surfaces depends

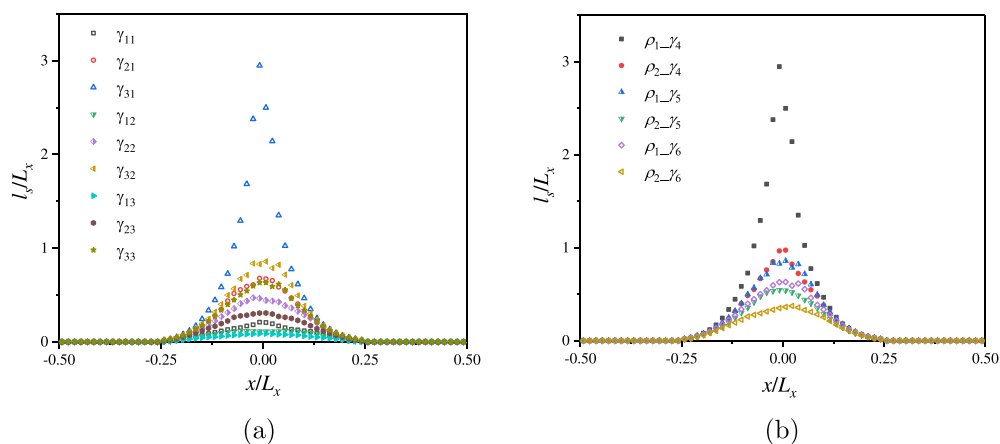


FIG. 10. The local slip length l_s at the LLI with increasing (a) friction coefficient of the working fluid γ_{ww} and (b) particle number density of the lubricant fluid ρ_l ($w = 31.55$). In the panel (a), the first subscripts "1," "2," and "3" in the legend represent $\gamma_{ww} = 2.0, 18.0,$ and 50.0 , respectively, while the second subscripts "1," "2," and "3" correspond to $\gamma_{ii} = 8.0, 18.0,$ and 32.0 , respectively. In the panel (b), the first symbols " ρ_1 " and " ρ_2 " denote $\rho_i = 3.24$ and 4.32 , respectively, whereas the second symbols " γ_4 ," " γ_5 ," and " γ_6 " correspond to $\gamma_{ii} = 8.0, 18.0,$ and 32.0 , respectively.

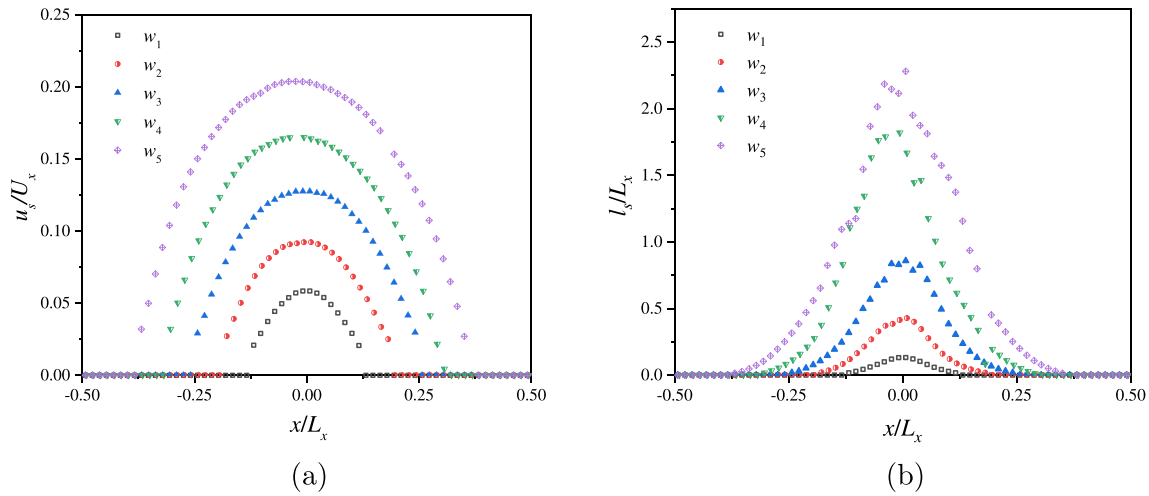


FIG. 11. (a) The local slip velocity u_s and (b) local slip length l_s at the LLI with different groove widths w ($w_1 = 15.60$, $w_2 = 23.57$, $w_3 = 31.55$, $w_4 = 39.52$, $w_5 = 47.50$, and $N = 17.62$).

on the fluid interface fraction. To study the effect of LISs on l_{es} , the flow of a heavy fluid over a light lubricant in a groove with different fluid interface fractions were simulated. Specifically, the system size L_x was fixed to 64.0 in the DPD units, the width of the groove (w) was varied from 15.6 to 47.8 in the DPD units to provide different fluid interface fractions (α) ranging from 0.25 to 0.75.

First, the local slip velocity and slip length for different values of w were calculated, as shown in Fig. 11. It can be seen that the local slip velocity (u_s) becomes larger for wider grooves [Fig. 11(a)]. Wider grooves lead to lower local shear stress (τ) and larger local slip length (l_s) [Fig. 11(b)]. For example, when w changes from 15.60 to 47.50 in the DPD units, the maximum u_s at the center of the LLI increases from $0.058 U_x$ to $0.20 U_x$, and the maximum l_s increases from $0.13 L_x$ to $2.15 L_x$.

In this numerical analysis, the effect of the viscosity ratio N on slip flow over LISs was considered. It was found that normalized profiles of u_s for different N and w nearly collapse into the elliptical function $u_s/u_s^{\max} = \sqrt{1 - (x/(w/2))^2}$, as shown in Fig. 12(a). When l_s is normalized by the product NL_x , the normalized profiles increase for wider grooves while they are less sensitive to the variation of N [Fig. 12(b)]. These results imply that the normalized slip length is mostly determined by the groove width, which agrees with conclusions of the Chang *et al.*'s study.³⁰

For the same flow conditions, the variation of the effective slip length (l_{es}) as a function of the fluid interface fraction (α) for the indicated values of the viscosity ratio (N) is shown in Fig. 13. It can be seen that for a fixed N , l_{es} increases with α for either the LLI over LISs

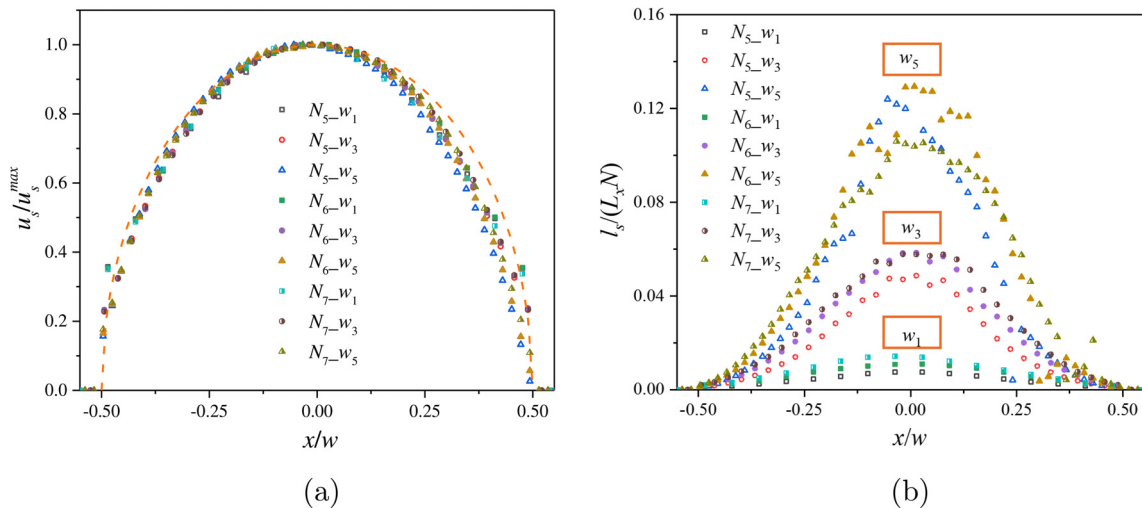


FIG. 12. Normalized profiles of (a) the local slip velocity u_s and (b) the local slip length l_s ($N_5 = 17.62$, $N_6 = 10.81$, and $N_7 = 8.74$; $w_1 = 15.60$, $w_3 = 31.55$, and $w_5 = 47.50$). The dashed orange curve in the panel (a) represents a fit using an elliptical function.

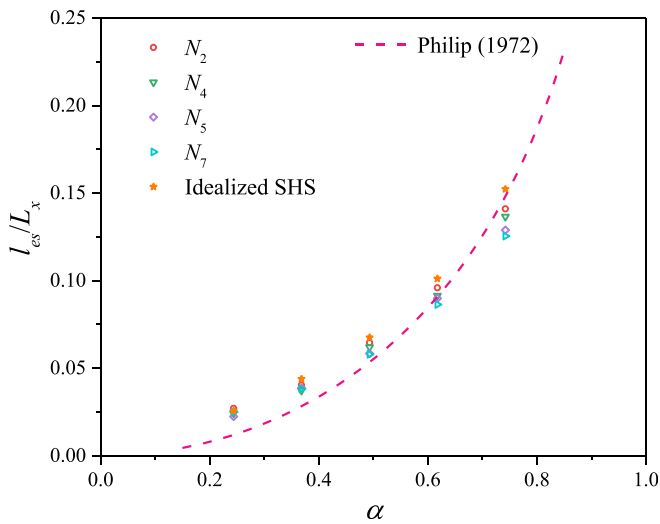


FIG. 13. Variation of the effective slip length l_{es} with increasing LLI (or GLI in the case of SHS) fractions α ($N_2 = 56.25$, $N_4 = 32.45$, $N_5 = 17.65$, and $N_7 = 8.74$). The dashed curve is given by Eq. (7).

or the GLI over SHSs. Note that l_{es} is rather insensitive to N for small values of α , whereas the effect of N becomes more pronounced at larger values of α (Fig. 13). For $\alpha = 0.25$, while N increases from 8.74 to 56.25, l_{es} only increases from $0.025 L_x$ to $0.027 L_x$. As α increases to a value of 0.75, l_{es} increases from $0.13 L_x$ to $0.14 L_x$ for the same variation of N . In addition, similar to the results for the local slip length in Fig. 9(b), l_{es} for LISs remains smaller than for the case of idealized SHS.

In Fig. 13, the results of the analytical prediction by Philip^{63,64} are included, which is given by

$$l_{es}^p = -\frac{L_x}{2\pi} \ln \left[\cos \left(\frac{\pi}{2} \alpha \right) \right], \quad (7)$$

where L_x is the system size and α represents the GLI fraction for idealized SHSs with empty grooves. It can be observed that except for $\alpha > 0.60$, the l_{es} values obtained from current mesoscopic simulations are greater than the theoretical predictions, given by Eq. (7). However, this discrepancy gradually decreases with increasing α . When α increases up to 0.75, the l_{es} values are below the predictions of Eq. (7). These results demonstrate that the assumption of zero stress used in Philip's study^{63,64} does not always hold for the case of LISs, and, instead, a finite slip or a hybrid boundary condition should be assumed.

The effect of the viscosity ratio N on the effective slip length (l_{es}) for different groove widths (w) is shown in Fig. 14. It can be seen that l_{es} becomes larger and more sensitive to N for wider grooves. Note that for a fixed w , the variation of l_{es} upon increasing N is not always monotonous. When $N < 10.81$ (the left gray region in Fig. 14), l_{es} is either constant or decreases with increasing N . In contrast, when $N > 10.81$ (the right orange region in Fig. 14), l_{es} monotonically increases with increasing N . Thus, the results in Fig. 14 indicate the range of system parameters required to maximize the effective slip flow over LISs.

As mentioned above, the effect of the viscosity ratio on the effective slip length l_{es} for flows over LISs was included in the analysis of

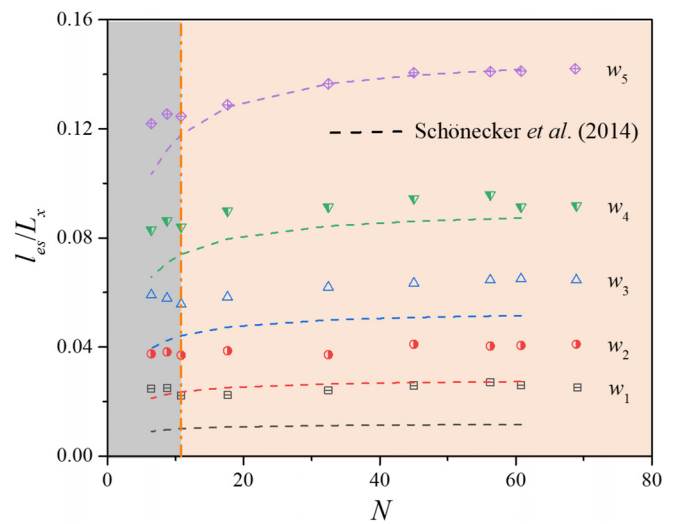


FIG. 14. The effective slip length l_{es} as a function of the viscosity ratio ($w_1 = 15.60$, $w_2 = 23.57$, $w_3 = 31.55$, $w_4 = 39.52$, and $w_5 = 47.50$). The dashed curves indicate theoretical predictions given by Eq. (8), the vertical dash-dotted line at $N = 10.81$ denotes a change in the functional dependence of l_{es} on N .

Schönecker *et al.*⁶² and the following expression for the effective slip length was derived:

$$l_{es}^s = -\frac{\ln \left[\cos \left(\frac{\pi}{2} \alpha \right) \right]}{2\pi + \frac{1}{2\alpha D_t N} \ln \left[\frac{1 + \sin \left(\frac{\pi}{2} \alpha \right)}{1 - \sin \left(\frac{\pi}{2} \alpha \right)} \right]}, \quad (8)$$

where D_t is the maximum value of the local slip length, α is the fluid interface fraction, and N denotes the viscosity ratio. The theoretical predictions based on Eq. (8) are indicated by dashed curves in Fig. 14. It was found that values of l_{es} obtained from current simulations are larger than predictions of Eq. (8); however, the difference is reduced with increasing groove width w . For $N = 32.45$, the difference between the computed l_{es} and the theoretical values obtained from Eq. (8) decreases from 53.47% to 7.60% as w increases from 15.60 to 39.52. Remarkably, upon further increasing w up to 47.50 in the DPD units, the difference between measured and predicted values becomes negligible for $N > 10.81$, as illustrated by the purple diamonds in Fig. 14.

After exploring a wide range of system parameters, two scenarios were identified for the variation of the effective slippage. Namely, when the groove width is relatively large, $w = 47.5$ in the DPD units, and the fluid interface fraction α is 0.75, then the Schönecker *et al.*'s analysis is applicable, i.e., the effective slip length increases significantly with the viscosity ratio. By contrast, in the case of narrow grooves, a free-shear assumption becomes more suitable, i.e., the effective slippage is only weakly dependent on the viscosity ratio. These conclusions are reflected in the transition between two slip modes. Although the local slip length gradually increases and becomes much larger than the system size at the central region of the LLI for higher viscosity ratios, the region of unbounded slip is relatively small for an LIS with a

low LLI fraction, and, as a result, its influence on the effective slip is small. On the other hand, when the size of the region with a large local slip length increases for an LIS with a high LLI fraction, the effective slip length becomes more sensitive to the viscosity ratio. Based on above simulations of flow over periodically grooved LISs, the results show that wider grooves with higher viscosity ratio could promote the effective slippage at the LLIs. This can be helpful for the design of LISs with an enhanced slip in microfluidic systems.

IV. CONCLUSIONS

In summary, a detailed analysis of flows over LISs was performed where the presence of LLI is essential for enhanced slip and drag reduction. By including a lateral friction coefficient in the standard MDPD method, a transverse MDPD scheme was employed to tune the viscosity of an MDPD fluid over a wide range. This transverse MDPD method was then used to investigate the behavior of the local and effective slip lengths for flows over periodically grooved LISs. In the simulation setup, the channel height was adjusted and, correspondingly, the contact angle of the LLI at the groove edge to make a flat LLI on top of the groove. The results indicated a formation of a shear-induced vortex flow inside the groove and the enhancement of the flow vorticity upon increasing viscosity ratio between the working and lubricant fluids. Two different local slip modes at the flat LLI were identified. At small values of the viscosity ratio, the local slip length and shear stress were both finite along the LLI, resulting in a finite slip boundary condition. By contrast, upon increasing viscosity ratio, the local shear stress at the central region of the LLI approaches zero, while the local slip length becomes much larger than the channel size, leading to a hybrid slip mode (or a hybrid slip boundary condition at high viscosity ratios).

The effective slip behavior can be broadly divided into two cases. For LISs with a higher LLI fraction, the effective slip length is a strong function of the viscosity ratio. When the fluid interface fraction is relatively small, the effective slip is less sensitive to the viscosity ratio. These changes are reflected in a transition between the two local slip modes. In the case of a hybrid slip boundary condition, the region of high slip is relatively small for the LIS with a low LLI fraction, leading to minor changes in the effective slip. When the region of a large local slip is expanded for a high LLI fraction, the effective slip length becomes more sensitive to the viscosity ratio. The simulation results of this study provides a comprehensive picture of the flow boundary conditions at LISs and can potentially be useful for the optimal design of structured interfaces with enhanced drag reduction.

ACKNOWLEDGMENTS

This work is sponsored by the National Natural Science Foundation of China (Grant Nos. 52071272, 51879218, and 12102358), the Natural Science Basic Research Program of Shaanxi Province (Program No. 2020JC-18), the Basic Frontier Project (Grant No. JCKY2018x18), the Innovation Foundation for Doctor Dissertation of Northwestern Polytechnical University (No. CX2021050), and the Fundamental Research Funds for the Central Universities (Grant No. 3102020HHZY030014).

AUTHOR DECLARATIONS

Conflict of Interest

The authors have no conflicts to disclose.

Author Contributions

Liuzhen Ren: Conceptualization (equal); Data curation (lead); Formal analysis (lead); Funding acquisition (supporting); Investigation (equal); Methodology (equal); Project administration (lead); Writing – original draft (lead); Writing – review and editing (equal). **Haibao Hu:** Formal analysis (supporting); Funding acquisition (lead); Project administration (lead); Supervision (lead). **Luyao Bao:** Formal analysis (supporting); Investigation (equal); Methodology (equal). **Nikolai Priezjev:** Formal analysis (equal); Writing – review and editing (equal). **Jun Wen:** Investigation (equal); Writing – review and editing (equal). **Luo Xie:** Funding acquisition (supporting); Investigation (equal); Writing – review and editing (equal).

DATA AVAILABILITY

The data that support the findings of this study are available from the corresponding authors upon reasonable request.

REFERENCES

- ¹M. Perlin, D. Dowling, and S. Ceccio, “Freeman scholar review: Passive and active skin-friction drag reduction in turbulent boundary layers,” *J. Fluid Eng.* **138**, 091104 (2016).
- ²S. Ceccio, “Friction drag reduction of external flows with bubble and gas injection,” *Annu. Rev. Fluid Mech.* **42**, 183–203 (2010).
- ³G. Tian, D. Fan, X. Feng, and H. Zhou, “Thriving artificial underwater drag-reduction materials inspired from aquatic animals: Progresses and challenges,” *RSC Adv.* **11**, 3399–3428 (2021).
- ⁴J. P. Rothstein, “Slip on superhydrophobic surfaces,” *Annu. Rev. Fluid Mech.* **42**, 89–109 (2010).
- ⁵C. Lee, C. H. Choi, and C. J. Kim, “Superhydrophobic drag reduction in laminar flows: A critical review,” *Exp. Fluids* **57**, 176 (2016).
- ⁶H. Park, C. H. Choi, and C. J. Kim, “Superhydrophobic drag reduction in turbulent flows: A critical review,” *Exp. Fluids* **62**, 229 (2021).
- ⁷D. G. Crowdy, “Superhydrophobic annular pipes: A theoretical study,” *J. Fluid Mech.* **906**, A15 (2021).
- ⁸D. G. Crowdy, “Slip length formulas for longitudinal shear flow over a superhydrophobic grating with partially filled cavities,” *J. Fluid Mech.* **925**, R2 (2021).
- ⁹D. Song, B. Song, H. Hu, X. Du, and J. P. Rothstein, “Effect of a surface tension gradient on the slip flow along a superhydrophobic air-water interface,” *Phys. Rev. Fluids* **3**, 033303 (2018).
- ¹⁰L. Ren, H. Hu, L. Bao, M. Zhang, J. Wen, and L. Xie, “Many-body dissipative particle dynamics study of the local slippage over superhydrophobic surfaces,” *Phys. Fluids* **33**, 072001 (2021).
- ¹¹H. Li, S. Ji, X. Tan, Z. Li, and H. Duan, “Effect of Reynolds number on drag reduction in turbulent boundary layer flow over liquid-gas interface,” *Phys. Fluids* **32**, 122111 (2020).
- ¹²Y. Xue, P. Lv, H. Lin, and H. Duan, “Underwater superhydrophobicity: Stability, design and regulation, and applications,” *Appl. Mech. Rev.* **68**, 030803 (2016).
- ¹³S. Huang, P. Lv, and H. Duan, “Morphology evolution of liquid-gas interface on submerged solid structured surfaces,” *Extreme Mech. Lett.* **27**, 34–51 (2019).
- ¹⁴P. Lv, Y. Xue, H. Liu, Y. Shi, and P. Xi, “Symmetric and asymmetric meniscus collapse in wetting transition on submerged structured surfaces,” *Langmuir* **31**, 1248–1254 (2015).
- ¹⁵D. Reholon and S. Ghaemi, “Plastron morphology and drag of a superhydrophobic surface in turbulent regime,” *Phys. Rev. Fluids* **3**, 104003 (2018).
- ¹⁶M. Xu, A. Grabowski, N. Yu, G. Kerezyte, J. Lee, B. Pfeifer, and C. J. Kim, “Superhydrophobic drag reduction for turbulent flows in open water,” *Phys. Rev. Appl.* **13**, 034056 (2020).
- ¹⁷M. Xu, G. Sun, and C. Kim, “Infinite lifetime of underwater superhydrophobic states,” *Phys. Rev. Lett.* **113**, 136103 (2014).

- ¹⁸W. Choi, M. Kang, J. Y. Park, H. E. Jeong, and S. J. Lee, "Enhanced air stability of superhydrophobic surfaces with flexible overhangs of re-entrant structures," *Phys. Fluids* **33**, 022001 (2021).
- ¹⁹J. Seo, R. García-Mayoral, and A. Mani, "Pressure fluctuations and interfacial robustness in turbulent flows over superhydrophobic surfaces," *J. Fluid Mech.* **783**, 448–473 (2015).
- ²⁰J. Seo, R. García-Mayoral, and A. Mani, "Turbulent flows over superhydrophobic surfaces: Flow-induced capillary waves, and robustness of air-water interfaces," *J. Fluid Mech.* **835**, 45–85 (2018).
- ²¹P. Du, J. Wen, Z. Zhang, D. Song, A. Ouahsine, and H. Hu, "Maintenance of air layer and drag reduction on superhydrophobic surface," *Ocean Eng.* **130**, 328–335 (2017).
- ²²C. Lee and C. J. Kim, "Underwater restoration and retention of gases on superhydrophobic surfaces for drag reduction," *Phys. Rev. Lett.* **106**, 014502 (2011).
- ²³T. J. Kim and C. Hidrovo, "Pressure and partial wetting effects on superhydrophobic friction reduction in microchannel flow," *Phys. Fluids* **24**, 112003 (2012).
- ²⁴P. Divya, R. Anoop, K. K. Varanasi, and G. H. McKinley, "Plastron regeneration on submerged superhydrophobic surfaces using in situ gas generation by chemical reaction," *ACS Appl. Mater. Interfaces* **10**, 33684 (2018).
- ²⁵D. Saranadhi, D. Chen, J. A. Kleingartner, S. Srinivasan, R. E. Cohen, and G. H. McKinley, "Sustained drag reduction in a turbulent flow using a low-temperature Leidenfrost surface," *Sci. Adv.* **2**, e1600686 (2016).
- ²⁶M. Shi, R. Das, S. Arunachalam, and H. Mishra, "Unexpected suppression of Leidenfrost phenomenon on superhydrophobic surfaces," *Phys. Fluids* **33**, 122104 (2021).
- ²⁷T. L. Liu and C. J. Kim, "Turning a surface superrepellent even to completely wetting liquids," *Science* **346**, 1096–1100 (2014).
- ²⁸H. Hu, J. Wen, L. Bao, L. Jia, D. Song, B. Song, G. Pan, M. Scaraggi, D. Dini, Q. Xue, and F. Zhou, "Significant and stable drag reduction with air rings confined by alternated superhydrophobic and hydrophilic strips," *Sci. Adv.* **3**, e1603288 (2017).
- ²⁹T. S. Wong, S. H. Kang, S. Tang, E. J. Smythe, B. D. Hatton, A. Grinthal, and J. Aizenberg, "Bioinspired self-repairing slippery surfaces with pressure-stable omniphobicity," *Nature* **477**, 443–447 (2011).
- ³⁰J. Chang, T. Jung, H. Choi, and J. Kim, "Predictions of the effective slip length and drag reduction with a lubricated micro-groove surface in a turbulent channel flow," *J. Fluid Mech.* **874**, 797–820 (2019).
- ³¹B. R. Solomon, K. S. Khalil, and K. K. Varanasi, "Drag reduction using lubricant-impregnated surfaces in viscous laminar flow," *Langmuir* **30**, 10970–10970 (2014).
- ³²B. J. Rosenberg, T. V. Buren, M. K. Fu, and A. J. Smits, "Turbulent drag reduction over air- and liquid- impregnated surfaces," *Phys. Fluids* **28**, 015103 (2016).
- ³³T. V. Buren and A. J. Smits, "Substantial drag reduction in turbulent flow using liquid-infused surfaces," *J. Fluid Mech.* **827**, 448–456 (2017).
- ³⁴M. A. Samaha and M. Gad-el Hak, "Slippery surfaces: A decade of progress," *Phys. Fluids* **33**, 071301 (2021).
- ³⁵S. Hardt and G. McHale, "Flow and drop transport along liquid-infused surfaces," *Annu. Rev. Fluid Mech.* **54**, 83–104 (2022).
- ³⁶I. Arenas, E. García, M. K. Fu, P. Orlandi, M. Hultmark, and S. Leonardi, "Comparison between super-hydrophobic, liquid infused and rough surfaces: A direct numerical simulation study," *J. Fluid Mech.* **869**, 500–525 (2019).
- ³⁷Y. Tuo, H. Zhang, X. Liu, and K. Song, "Drag reduction with different liquids on slippery liquid-infused porous surface," *Surf. Eng.* **37**, 1215–1222 (2021).
- ³⁸J. L. Sang, H. N. Kim, W. Choi, G. Y. Yoon, and E. Seo, "A nature-inspired lubricant-infused surface for sustainable drag reduction," *Soft Matter* **15**, 8459–8467 (2019).
- ³⁹J. S. Wexler, I. Jacobi, and H. A. Stone, "Shear-driven failure of liquid-infused surfaces," *Phys. Rev. Lett.* **114**, 168301 (2015).
- ⁴⁰P. Baumli, H. Teisala, H. Bauer, D. Garcia-Gonzalez, V. Damle, F. Geyer, M. D'Acunzi, A. Kaltbeitzel, H. J. Butt, and D. Vollmer, "Flow-induced long-term stable slippery surfaces," *Adv. Sci.* **6**, 1900019 (2016).
- ⁴¹J. H. Kim and J. P. Rothstein, "Delayed lubricant depletion on liquid-infused randomly rough surfaces," *Exp. Fluids* **57**, 81 (2016).
- ⁴²H. N. Kim, S. J. Kim, W. Choi, S. HJ, and J. L. Sang, "Depletion of lubricant impregnated in a cavity of lubricant-infused surface," *Phys. Fluids* **33**, 022005 (2021).
- ⁴³E. S. Asmolov, T. V. Nizkaya, and O. I. Vinogradova, "Enhanced slip properties of lubricant-infused grooves," *Phys. Rev. E* **98**, 033103 (2018).
- ⁴⁴A. A. Hemedá and H. V. Tafreshi, "Liquid-infused surfaces with trapped air (LISTA) for drag force reduction," *Langmuir* **32**, 2955–2962 (2016).
- ⁴⁵P. B. Warren, "Vapor-liquid coexistence in many-body dissipative particle dynamics," *Phys. Rev. E* **68**, 066702 (2003).
- ⁴⁶P. Espanol and P. B. Warren, "Perspective: Dissipative particle dynamics," *J. Chem. Phys.* **146**, 150901 (2017).
- ⁴⁷Z. Li, X. Bian, Y. Tang, and G. E. Karniadakis, "A dissipative particle dynamics method for arbitrarily complex geometries," *J. Comput. Phys.* **355**, 534–547 (2018).
- ⁴⁸C. Wang, X. Wu, H. Zhang, P. Hao, and X. Zhang, "A many-body dissipative particle dynamics study of eccentric droplets impacting inclined fiber," *Phys. Fluids* **33**, 042001 (2021).
- ⁴⁹Z. Li, G. Hu, Z. Wang, Y. Ma, and Z. Zhou, "Three dimensional flow structures in a moving droplet on substrate: A dissipative particle dynamics study," *Phys. Fluids* **25**, 072103 (2013).
- ⁵⁰C. Junghans, M. Praprotnik, and K. Kremer, "Transport properties controlled by a thermostat: An extended dissipative particle dynamics thermostat," *Soft Matter* **4**, 156–161 (2008).
- ⁵¹L. Ren, H. Hu, L. Bao, L. Xie, and J. Wen, "Transverse effect on liquid viscosity: A many-body dissipative particle dynamics simulation study," *Phys. Fluids* **34**, 012006 (2022).
- ⁵²A. Mishra, A. Hemedá, M. Torabi, J. Palko, S. Goyal, D. Li, and Y. Ma, "A simple analytical model of complex wall in multibody dissipative particle dynamics," *J. Comput. Phys.* **396**, 416–426 (2019).
- ⁵³J. Zhao, S. Chen, K. Zhang, and Y. Liu, "A review of many-body dissipative particle dynamics (MDPD): Theoretical models and its applications," *Phys. Fluids* **33**, 112002 (2021).
- ⁵⁴C. Lin, S. Chen, P. Wei, L. Xiao, D. Zhao, and Y. Liu, "Dynamic characteristics of droplet impact on vibrating superhydrophobic substrate," *Phys. Fluids* **34**, 052005 (2022).
- ⁵⁵C. Lin, S. Chen, L. Xiao, and Y. Liu, "Tuning drop motion by chemical chessboard-patterned surfaces: A many-body dissipative particle dynamics study," *Langmuir* **34**, 2708–2715 (2018).
- ⁵⁶J. A. Backer, C. P. Lowe, H. C. J. Hoeflsloot, and P. D. Iedema, "Poiseuille flow to measure the viscosity of particle model fluids," *J. Chem. Phys.* **122**, 154503 (2005).
- ⁵⁷S. K. Ranjith, B. Patnaik, and S. Vedantam, "No-slip boundary condition in finite-size dissipative particle dynamics," *J. Comput. Phys.* **232**, 174–188 (2013).
- ⁵⁸J. Alejandre, D. J. Tildesley, and G. A. Chapela, "Molecular dynamics simulation of the orthobaric densities and surface tension of water," *J. Chem. Phys.* **102**, 4574–4583 (1995).
- ⁵⁹X. Wang, K. P. Santo, and A. V. Neimark, "Modeling gas-liquid interfaces by dissipative particle dynamics: Adsorption and surface tension of cetyl trimethyl ammonium bromide at the air-water interface," *Langmuir* **36**, 14686–14698 (2020).
- ⁶⁰M. Arienti, W. Pan, X. Li, and G. Karniadakis, "Many-body dissipative particle dynamics simulation of liquid/vapor and liquid/solid interactions," *J. Chem. Phys.* **134**, 204114 (2011).
- ⁶¹S. Plimpton, "Fast parallel algorithms for short-range molecular-dynamics," *J. Comput. Phys.* **117**, 1–19 (1995).
- ⁶²C. Schonecker, T. Baier, and S. Hardt, "Influence of the enclosed fluid on the flow over a microstructured surface in the Cassie state," *J. Fluid Mech.* **740**, 168–195 (2014).
- ⁶³J. R. Philip, "Flows satisfying mixed no-slip and no-shear conditions," *Z. Angew. Math. Phys.* **23**, 353–372 (1972).
- ⁶⁴J. R. Philip, "Integral properties of flows satisfying mixed no-slip and no-shear conditions," *Z. Angew. Math. Phys.* **23**, 960–968 (1972).